Graphical abstract

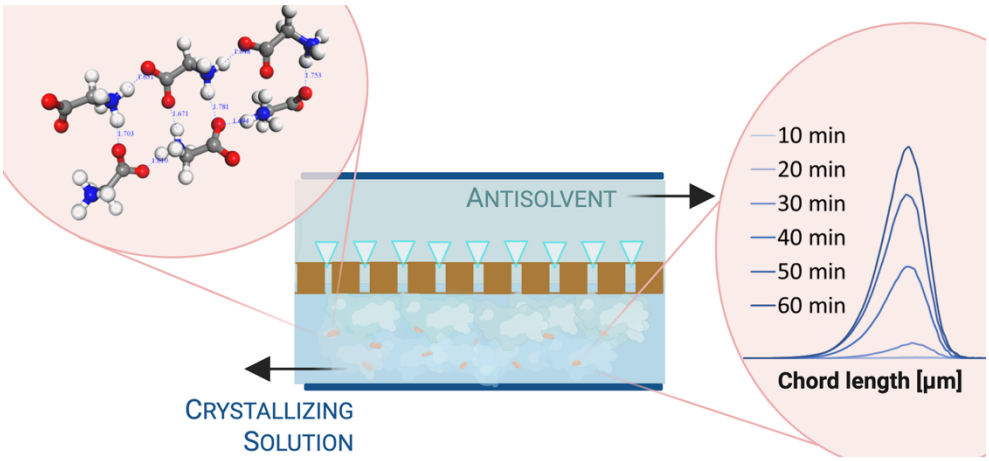

Modulating Crystal Polymorphism via Membrane-Regulated Supersaturation: An Experimental and Molecular Dynamics Simulation Study

Sara Chergaoui[1,2,3*], Elena Tocci[3], Carmen Rizzuto[3], Giuseppe Prenesti[3,4], Damien P. Debecker[2,5], Tom Leyssens[2,5], Patricia Luis[1,2]

[1]*Institute of Mechanics, Materials and Civil Engineering - Materials & Process Engineering (iMMC-IMAP), UCLouvain, Place Sainte Barbe 2, 1348 Louvain-la-Neuve, Belgium*

[2]*Research & Innovation Centre for Process Engineering (ReCIPE), UCLouvain, Place Sainte Barbe 2, 1348 Louvain-la-Neuve, Belgium*

[3]*Institute on Membrane Technology (CNR-ITM), via P. Bucci 17/C, Rende, (CS) 87036, Italy*

[4]*Department of Computer Engineering, Modelling, Electronics and System Engineering (DIMES), University of Calabria (UNICAL), Via P. Bucci, Cubo 42C, Rende (CS) 87036, Italy*

[5]*Institute of Condensed Matter and Nanosciences (IMCN), UCLouvain, Place Louis Pasteur 1, 1348 Louvain-la-Neuve, Belgium*

*Corresponding author:

Sara Chergaoui:

Telephone: (+32)4928784209

Email address: sara.chergaoui@uclouvain.be

Postal Address: Place Sainte Barbe 2, 1348 Louvain-la-Neuve, Belgium

Abstract

Hypothesis

Crystal properties are essential in determining the functionality of final products in pharmaceutical and food applications. This study hypothesizes that membrane-assisted antisolvent crystallization (MAAC) can regulate supersaturation profiles to influence polymorph selection and crystal growth kinetics in glycine crystallization. By using polyvinylidene fluoride (PVDF) membranes to control ethanol diffusion, it is expected that MAAC can promote the formation of specific polymorphs, particularly α-glycine, through modulation of molecular self-assembly pathways.

Experiments

To test this hypothesis, MAAC was implemented with PVDF membranes to generate stable supersaturation conditions during glycine crystallization. The membrane served as a mass transfer barrier, enabling controlled ethanol diffusion and allowing for detailed analysis of crystal size and polymorphic distribution. Experimental crystallization outcomes were complemented by molecular dynamics (MD) simulations of glycine-water-ethanol systems at three supersaturation levels (S = 0.74, 1.35, and 2.39). These simulations were used to investigate the formation of molecular aggregates and hydrogen bonding patterns, and to quantify nucleation induction times under varying supersaturation conditions.

Findings

MAAC enabled the formation of α-glycine with a narrow chord length distribution and a mean size of 86 μm. MD simulations revealed that cyclic glycine dimers, precursors to α-glycine, formed at lower supersaturation, while disordered aggregates associated with β-glycine dominated at higher supersaturation. Ethanol was shown to modulate hydrogen bonding and self-assembly, influencing polymorphic outcomes. Induction times decreased significantly with increasing supersaturation, from 1.9 ns to less than 100 ps, highlighting the kinetic control enabled by membrane-regulated crystallization.

Keywords – Molecular dynamics; antisolvent crystallization; Hydrogen bonds; Polymorphism; Membrane-assisted crystallization (MAAC).

1. Introduction

Membrane-assisted crystallization offers a novel interface-driven approach to control supersaturation during crystallization [1,2]. Unlike bulk antisolvent methods, membrane-assisted antisolvent crystallization (MAAC) enables gradual antisolvent diffusion across membrane interfaces, creating spatially resolved supersaturation profiles that influence nucleation and growth kinetics [3]. This controlled mass transfer mitigates supersaturation spikes, allowing for a more predictable and uniform crystallization process [4].

Polymorphism, affects drug solubility, bioavailability, and stability, making the precise control over crystallization processes a critical challenge [5]. While antisolvent crystallization is widely used in pharmaceutical processing, a rapid and uncontrolled mixing can result in high supersaturation bursts, leading to undesired polymorphic forms or uncontrolled crystal size distributions [6]. MAAC was then chosen in this study, primarily to establish well-defined supersaturation conditions for studying solution-phase crystallization. Understanding the influence of such controlled conditions on nucleation mechanisms and polymorph selection is essential for optimizing crystallization processes in pharmaceutical and industrial applications [7,8].

Glycine, the simplest amino acid, serves as an ideal model system for studying crystallization due to its well-characterized polymorphism and relevance in pharmaceuticals, biomaterials, and industrial processes [9,10]. It exists in multiple polymorphic forms (α, β, and γ), each exhibiting distinct hydrogen bonding arrangements that influence solubility and stability. Controlling glycine crystallization is critical, as its polymorphic form determines its bioavailability and functionality in pharmaceutical formulations. Additionally, glycine plays a key role in biochemical pathways [11,12], further highlighting its significance in material science and drug development.

Both molecular dynamics (MD) simulations and experimental approaches are essential to understanding these mechanisms [13–15]. MD simulations offer molecular-scale insights that are difficult to capture with macroscopic experimental techniques, such as the self-assembly of glycine molecules, their interactions with solvent molecules, and the transition from solution to crystalline phases [16]. Prior MD studies have explored glycine crystallization in bulk systems, showing that solvent composition influences polymorphic selection [17]. For example, Yani *et al.*, demonstrated that glycine molecules exist as monomers or open dimers in aqueous solutions [13]. Chen *et al*., investigated antisolvent crystallization using methanol and found that cyclic

glycine dimers were more prevalent in methanol-water mixtures, affecting polymorph selection [18]. However, these studies focused on homogeneous antisolvent crystallization rather than membrane-regulated. Thus, the impact of membrane-regulated supersaturation on glycine nucleation remains an open question.

To address this gap, this study combines membrane-assisted crystallization experiments and MD simulations to explore how controlled supersaturation, achieved through membrane-regulated antisolvent diffusion, influences glycine nucleation and polymorph selection. The membrane is employed not as a variable under study, but as a tool to achieve a gradual and spatially controlled antisolvent diffusion, enabling the fine modulation of supersaturation. Under these controlled conditions, the study aims to clarify how glycine nucleation pathways and polymorphic outcomes are influenced by the supersaturation profile. Experimentally, the work focuses on analyzing the effect of membrane-controlled ethanol diffusion on nucleation mechanisms, crystal growth dynamics, and polymorph selection, supported by in-situ monitoring (FBRM) and structural analysis (XRD). Molecular dynamics simulations are used to probe the early-stage aggregation behavior of glycine at the molecular level, revealing how different supersaturation regimes drive the formation of ordered clusters or disordered aggregates. By bridging experimental observations with molecular-level insights from MD simulations, this study aims to establish a clearer mechanistic understanding of crystal nucleation under controlled antisolvent crystallization conditions. The insights obtained may inform the design of next-generation membranes and crystallization protocols and could be extended to more complex pharmaceutical compounds where precise polymorph control is critical for drug stability and bioavailability.

2. Materials and Methods

2.1. Material

Glycine (Sigma-Aldrich, Belgium, 99% purity) was dissolved in ultrapure water (laboratory, 18.2 MΩcm) at a concentration of 20 wt.% to formulate the crystallizing solution. Pure ethanol (99%) was purchased from VWR (Belgium). Flat sheet membranes made of Polyvinylidene fluoride with a pore size of 0.2 µm, were purchased from Merck (Belgium).

2.2. Experimental methods

2..2.1. Membrane-assisted antisolvent crystallization

A custom-built experimental setup (Figures 1 and S1) was used to evaluate membrane-assisted antisolvent crystallization (MAAC). A membrane module with an active area of 12×10 cm was provided by DeltaE Srl membrane module (Italy). A model solution was prepared by dissolving glycine in ultrapure water at a concentration of 20 wt% and a temperature of 25 °C. This solution was circulated by a gear pump through the lower membrane cell at 100 mL/min (ColeParmer, Belgium). Pure ethanol was used as antisolvent solution and was circulated through the membrane module upper cell using the gear pump Verder, Belgium, at 150 mL/min. The flow rates were selected based on previous optimization studies [19–21] to prevent undesirable reverse flow across the membrane. When ethanol contacts the hydrophobic PVDF membrane, its surface properties can change, increasing the risk of water permeation. Maintaining a slightly higher antisolvent flow rate compared to the crystallizing solution minimizes this risk and ensures stable, controlled mass transfer during MAAC. The Focused Beam Reflectance Measurement (FBRM) probe was used to accurately detect the crystal chord length evolution during experimental operation; meanwhile, a balance continuously recorded the mass of the antisolvent solution as it permeated through the membrane over time.

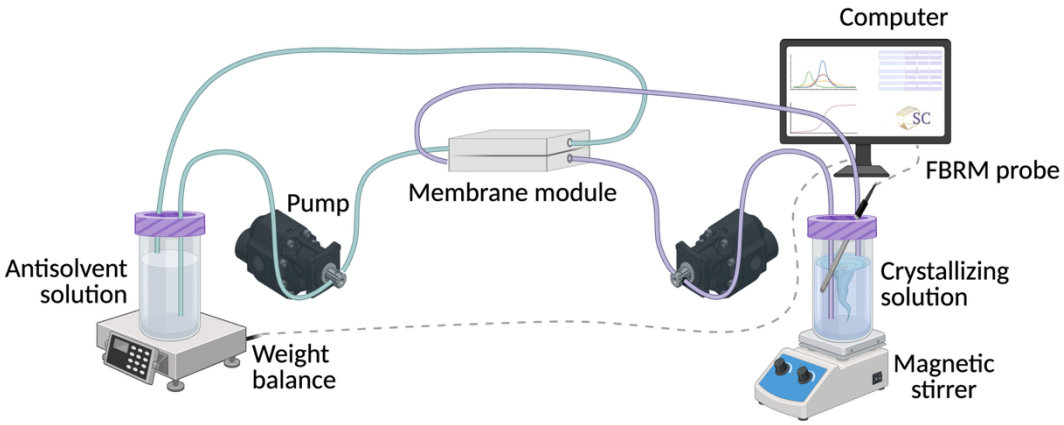

Fig. 1 Schematic of the set-up used to evaluate membrane-regulated crystallization. An in-line FBRM probe was installed at 45˚ in the crystallizing solution to continuously track the chord length.

Antisolvent permeation was tracked over time to assess the transmembrane mass transfer, quantified as the net flux (Eq. 1). The ethanol content in the crystallizing solution was determined from the total solution mass and the ethanol weight fraction measured by gas chromatography:

$$J = \frac{1}{A}\frac{w_{as}(t_{i+1}) - w_{as}(t_i)}{t_{i+1} - t_i} \qquad \text{(Eq. 1)}$$

J designates the net transmembrane flux of the antisolvent ethanol in kg/m^{2}s, A the effective area of the membrane (0.012 m^2), t_i the operation time i in s, and w_{as} the weight of the antisolvent in kg.

The ethanol content was measured every 10 minutes over a 2-hour experimental period using a Thermo Scientific™ TRACE 1300 Gas Chromatograph (GC) equipped with a flame ionization detector (FID). Samples were taken from both the crystallizing solution and the antisolvent side. The ethanol concentration in the crystallizing solution was used to assess supersaturation formation, while change in the antisolvent side was verified to check for the absence of reverse membrane permeation. Each retrieved sample (0.5 g) was mixed with an equal amount of 0.01 wt.% acetonitrile solution before analysis. Each sample was analyzed at least twice using the GC, with data interpretation based on the calibration curve shown in Fig. S2.

2.2.2. Characterization of Membranes and Crystals

The membrane morphology was analyzed using a Scanning Electron Microscope (SEM) (Zeiss, ULTRA). To obtain a clean cross-section, the membrane sample was immersed in liquid nitrogen. Before SEM imaging, a thin layer of gold was sputter-coated onto the samples (Balzers Union FL 9460 BALZERS SCD 030) to ensure conductivity. Membrane surface roughness was analyzed using Atomic Force Microscopy (AFM) with the Dimension Icon and MultiMode 8 systems (Bruker Corp., USA), operated in PeakForce Tapping®-QNM mode with a factory-calibrated RTESPA-300–30 probe. AFM scans were acquired at dimensions of 10×10 and 3×3 μm, with Samples per Line parameter set to 256. The scan rate and amplitude parameters were respectively set to 0.5 kHz and 20 nm.

Glycine solubility in water-ethanol was obtained from our previous work (Fig. S3) [19]. Crystals were retrieved from the crystallizing solution after each MAAC experiment and air-dried overnight. To ensure conductivity for characterization, a thin gold coating was applied to the crystal samples using a sputter coater (BALZERS UNION FL 9460 BALZERS SCD 030) under vacuum conditions. The crystalline structure of the obtained glycine crystals was

investigated via X-ray diffraction (XRD), conducted over a 2θ range of 10° to 100° using a Bruker D8 Advance diffractometer equipped with Cu Kα radiation (λ = 1.5406 Å). Crystal growth in solution was monitored using a focused beam reflectance measurement (FBRM) probe (Mettler Toledo, Belgium). This in-line monitoring system enabled real-time tracking of chord length distribution, capturing measurements every 10 seconds to provide a precise insight into the crystallization process.

2.3. Computational methods

Molecular dynamics simulations were conducted to explore the earliest stages of glycine aggregation under solution conditions representative of those achieved experimentally through membrane-assisted antisolvent crystallization. While the PVDF membrane was not explicitly modeled at the molecular level in the main simulations, the focus on bulk glycine-water-ethanol mixtures at well-defined supersaturation levels allowed us to capture key self-assembly mechanisms influenced by membrane-controlled ethanol diffusion. Additionally, an optimized model incorporating PVDF was developed and discussed in Section 3.2.7 to provide further insight into membrane-specific effects.

Classical MD simulations were carried out on aqueous solutions comprising glycine in the ethanol-water mixture at a ratio from undersaturated (S=0.74) to supersaturated (S=1.35 and 2.39). The forces were computed in Gromacs 5.1.2 software [22] using the force field opls-aa [23] which has a good library of organic solvents and is optimized for liquid simulations and validated for glycine simulations [18,24]. Visual Molecular Dynamics (VMD) 1.9.3 software package was used to visualize the structures [25].

The glycine molecule was imported from the supplementary files by Terterov *et al.*[26], in its zwitterionic form $NH_3^+CH_2COO^-$ (Fig. S4), given the solution pH was 7. The 3-point spc216 model was used for water molecules [27]. Ethanol molecules were modelled using the OPLS-AA parameters.

Periodic boundary conditions were imposed in all three spatial directions. A cut-off radius of 1.2 nm was used for both electrostatic and van der Waals interactions, with long-range electrostatics computed using the Particle-Mesh Ewald (PME) method [28]. All bonds were constrained with the LINCS algorithm [29]. Each simulation box has dimensions of 4.5×4.5×4.5 nm, which provides a schematic representation of the molecular study of the Glycine-Ethanol-Water system used in MD simulations (Fig. S5). The simulations were run on a 32-core CPU server (CINECA-ISCRA project).

All systems were equilibrated with an energy minimization using the steepest descent algorithm until the maximum force on any atom was below 1000 kJ mol^{-1} nm^{-1} or a maximum number of 50000 steps was reached, whichever occurred first. This criterion ensured removal of any steric conflicts before starting dynamics. Following minimization, each system was equilibrated in the NPT ensemble (constant pressure, number of molecules and temperature) at 300 K and 0.1 MPa. Equilibration was continued until the box volume and density reached stable average values, typically within the first 20-30 ns. We monitored the time evolution of these quantities and ensured that no systematic drift was observed over extended time intervals. Calculations were carried out with the Nosé–Hoover thermostat (τ = 1 ps) and the Parrinello–Rahman barostat (τ = 3 ps), respectively [30–32]). Production simulations were then run for at least 500 ns to capture the early stages of glycine aggregation, including dimer formation, and hydrogen-bond network rearrangements. Test runs indicated that shorter trajectories could miss relevant aggregation events, particularly at lower supersaturation. The 500 ns window thus represents a compromise between computational cost and the need to observe statistically meaningful aggregation behavior. Each simulation run was repeated at least twice to confirm reproducibility; quantitative uncertainty analysis was not performed.

In this work, supersaturation S is defined as:

$$S = \frac{c}{c_{sat}} \qquad \text{(Eq. 2)}$$

where c is the concentration of glycine in solution and c_{sat} is the solubility of glycine in the corresponding water–ethanol mixture (taken from our previous experimental solubility measurements). Values of $S<1$ correspond to undersaturated solutions, while $S>1$ identify supersaturated conditions. The three values S = 0.74, 1.35, and 2.39 were chosen to sample:

(i) a clearly undersaturated regime (S = 0.74),

(ii) a moderately supersaturated regime relevant to MAAC experiments (S = 1.35), and

(iii) a highly supersaturated regime representative of fast antisolvent mixing (S = 2.39).

For each S value, the number of glycine molecules in Table 1 was determined by converting the target concentration into a discrete number of molecules within the simulation box. Starting from a cubic box of initial size 4.5 × 4.5 × 4.5 nm^3, we first estimated the box volume and then calculated the number of glycine molecules corresponding to the desired solute concentration. Water and ethanol molecules were then added to match a realistic liquid density and to reproduce the target solvent composition at that supersaturation level. The final densities

obtained after NPT equilibration are consistent with typical values for aqueous ethanol mixtures at 300 K and 0.1 MPa. Table 1 summarizes the molecular composition of each system.

Table 1: The composition of the simulation boxes in glycine, ethanol, and water molecules.

	S=0.74	S=1.35	S=2.39	S=1.35 (No Ethanol)
N. Glycine	27	53	108	108
N. Ethanol	101	101	101	0
N. Water	1000	1000	1000	1000

The Radial Distribution Function $g_{AB}(r)$ was calculated between NH_3^+ and COO^- groups to analyze the microstructure of glycine using the g_rdf utility of the GROMACS package. The pair correlation function g_{AB}(r) describes the probability of finding a pair of particles A and B separated by a distance $r(dr)$ normalized by the probability expected for a completely random distribution at the same particle density (Eq. 3):

$$g_{AB}(r) = \frac{V\left\langle \sum_{i \neq j} \delta(r - |r_{Ai} - r_{Bj}|) \right\rangle}{(N_A N_B - N_{AB}) 4\pi r^2 \, dr} \qquad \text{(Eq. 3)}$$

A and B denote two distinct types of particles within a system of volume V, containing N_A and N_B particles of type A and B, respectively. N_{AB} represents particles classified as both A and B. The position vectors r_{Ai} and r_{Bj} correspond to particles A and B, respectively, and the distance between them is given by $|r_{Ai} - r_{Bj}|$. The term $\delta\left(r - |r_{Ai} - r_{Bj}|\right)$ is assigned a value of 1 if $\left(r - |r_{Ai} - r_{Bj}|\right) \leq dr$; meaning, when the deviation between the actual and target distance between the two particles is less than a tolerance factor dr. The NH_3^+–COO^- radial distribution function was computed including both intramolecular and intermolecular pairs, providing the total g(r) that describes all hydrogen-bonding environments of glycine in solution.

The Density-Based Spatial Clustering of Applications with Noise (DBSCAN) algorithm [33] was employed to detect glycine crystals (defined as clusters). In this context, a cluster refers to a group of mutually connected glycine molecules, as defined by the DBSCAN algorithm. The core principle of DBSCAN is to identify regions with high object density (glycine) that are separated by regions of lower density. This is achieved by considering two

key parameters: the number of glycine molecules, denoted as η, and the distance ε, which represents the search radius in each iteration (Fig. S6). The DBSCAN algorithm was applied to structures extracted from the trajectory every 100 ps. The growth rate of formed crystals at the Angstrom scale was elaborated for a qualitative study between empirical and MD simulation approaches. Yasuoka-Matsumoto method was utilized to analyse the temporal evolution of crystals [34,35].

The orientational order parameter was calculated using two intramolecular reference vectors (Fig. S7) connecting the two carbon atoms (Cα and Cα) and connecting the Cα carbon to the nitrogen atom (Cα and N).

Using the same distance cutoff between Cα - Cα atoms employed for DBSCAN, the orientational order parameter P_2 (Eq. 4) was computed for each molecular pair based on the angle formed between the corresponding vectors of the two glycine molecules (Cα-C/ Cα-C and Cα-N/ Cα -N).

$$P_2 = \langle \frac{1}{2}(3cos^2\,\theta - 1 \rangle \qquad \text{(Eq. 4)}$$

where θ is the angle formed between the two vectors of two different glycine molecules. P_2=1 corresponds to perfect orientational alignment, P_2=-0.5 indicates a strictly perpendicular arrangement, whereas P_2=0 reflects an isotropic (random) orientational distribution.

3. Results and Discussion

3.1. Glycine crystallization under membrane-regulated supersaturation

Our previous work and recent advances in membrane-assisted antisolvent crystallization (MAAC) have established that gradual, membrane-regulated antisolvent addition enables precise control over supersaturation profiles, creating tunable and reproducible environments for glycine crystallization [19–21]. Our previous work and recent advances in MAAC have established that gradual, membrane-regulated antisolvent addition enables precise control over supersaturation profiles, creating tunable and reproducible environments for glycine crystallization [3,6]. In MAAC, the membrane acts as a selective mass transfer barrier, allowing for the fine modulation of antisolvent flux and, consequently, the supersaturation rate, an essential parameter for directing nucleation and crystal growth.

Despite these advances, the fundamental mechanisms by which the membrane influences crystallization remain incompletely understood. As illustrated in Fig. 2, the spatial location of antisolvent introduction, whether within the boundary layer (Fig. 2a) or at the membrane surface/pore interface (Fig. 2b) can dictate distinct nucleation regimes. When antisolvent transport is limited to the boundary layer, homogeneous nucleation dominates, characterized by longer induction times and lower nucleation rates, as supported by both experimental and simulation studies [3,13,18]. Here, process parameters such as solution velocity and antisolvent permeation rate, which can be tuned via membrane properties or operating conditions, are critical for controlling crystallization kinetics [19,21].

Conversely, when nucleation occurs at or within the membrane pores, particularly at the nanoscale, heterogeneous nucleation is promoted, with the membrane's cross-sectional structure, surface chemistry, and the local antisolvent/solvent ratio playing pivotal roles [16,36]. This duality in nucleation pathways is a unique feature of MAAC and underpins its potential for selective polymorph control, as recently demonstrated for glycine and other small molecules [1,4,5,36].

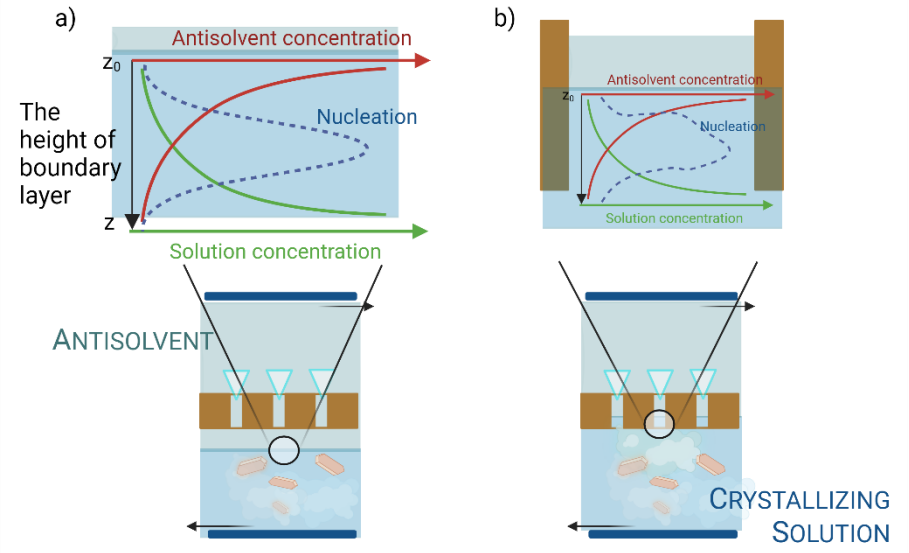

Fig. 2 Representation of the boundary layer conditions depending on the antisolvent transmembrane flux: either nucleation is solely related to the direct contact of the antisolvent and crystallizing solution (a) or is additionally impacted by the heterogeneous nucleation from the membrane surface (b).

In this study, we employed a hydrophobic PVDF membrane with a symmetric sponge-like structure to systematically investigate these regimes. Real-time FBRM monitoring enabled precise tracking of chord length evolution, while molecular dynamics simulations provided molecular-level insight into the self-assembly and nucleation mechanisms under different supersaturation conditions. This integrated approach not only advances the mechanistic understanding of membrane-regulated crystallization but also aligns with the journal's emphasis on fundamental principles and conceptually novel applications in colloid and interface science.

3.1.1 Crystal properties

Crystals recovered at the end of each MAAC experiment were characterized by XRD and focused beam reflectance measurements to determine polymorphic form and chord length distribution (Fig. 3). The final crystal morphology corresponded to the expected hexagonal shape of α-Glycine (Fig. 3a). In our previous MAAC study, using L-serine-water-ethanol as model solution in a polypropylene membrane-based crystallizer, the crystal size grew gradually from 26 to 110 μm (Fig. S8) with the incremental of antisolvent concentration in the crystallizing solution. The crystal morphology evolved from hexagonal plates at initial appearance in solution to an orthorhombic morphology by the end of experiment [20].

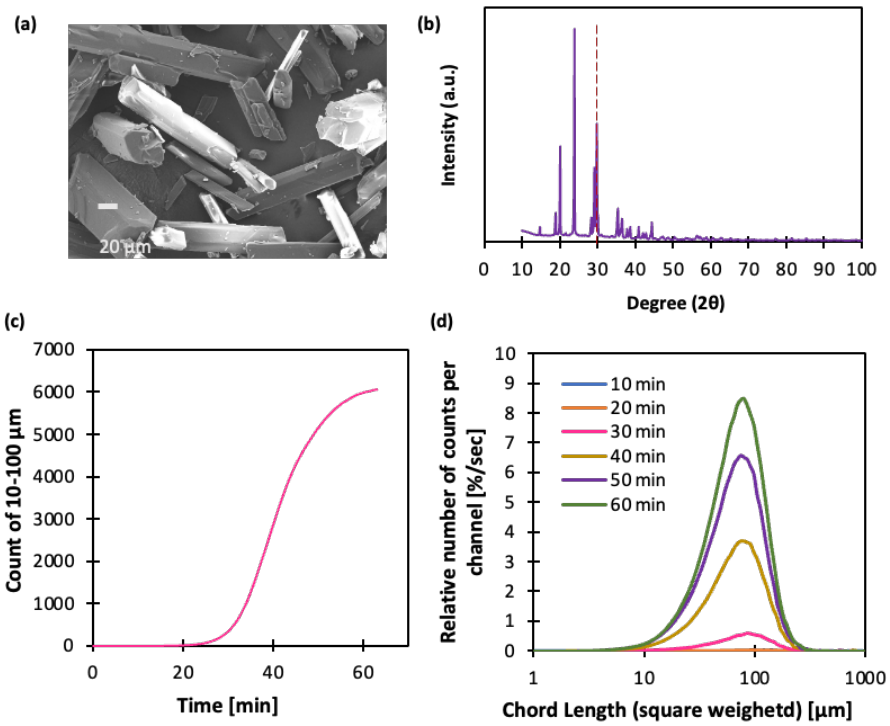

Fig. 3 Crystal shape and morphology obtained with MAAC (a), crystalline structure (b), FBRM chord count with time (c), and chord length distribution (d). Values represent mean measurements from three replicate MAAC experiments. The standard deviation for chord length was ±10 µm, and for chord count ±8%.

The diffraction peak at 2θ ≈ 30° (Fig. 3b) confirmed the predominance of the α-glycine (0 4 0) plane, consistent with previous studies indicating that gradual ethanol diffusion favors α-polymorph formation. Throughout the experimental duration, the chord count and chord length distribution were tracked continuously (Fig. 3c). The increased membrane-solution interface enhances antisolvent contact, compared to conventional stirred-tank crystallizers. This large surface contact has been known to be advantageous in membrane-based processes. The convective flow of the antisolvent through the membrane pores into the crystallizing solution initiates crystallization. As crystals form and grow, they remain in contact with the antisolvent through the membrane flow channels. The membrane pores create thousands of localized environments that mimic the behavior of two-jet systems [37].

The mean chord length of glycine crystals was 86 µm, with a narrow, unimodal distribution, suggesting that membrane-controlled ethanol diffusion minimizes secondary nucleation events, promoting stable crystal growth. The peak intensity increased over time (Fig.

3d), meaning more crystals are detected at the dominant size. The width of the distribution did not change drastically, indicating that crystal size variation was relatively stable. Since the peak position increased without significant broadening, the system likely experienced growth-dominated crystallization rather than extensive nucleation. If secondary nucleation was significant, small particle fractions (which was not apparent here) would have been observed.

3.1.2. Membrane properties and antisolvent mass transfer

While the membrane is not the focus of this study, its structural and functional integrity was assessed to confirm its suitability as a stable medium for achieving controlled supersaturation during glycine crystallization. Porous PVDF membranes with a sponge-like cross-sectional structure (Fig. 4) were used to evaluate glycine crystallization through MAAC. Our previous work investigated the key parameters involved in crystallization using polypropylene membranes [21]. The variation of temperature, solution flow rates, and antisolvent weight fraction impacted antisolvent transmembrane flux. These results were considered to determine the antisolvent and solution flow rates while operating at room temperature.

The SEM imaging (Fig. 4) confirmed that the membrane structure remained intact after the crystallization process, with no significant changes in morphology, neither on the surface nor on the cross-section. There could slightly be some variation at the surface functional groups, or presence of nanocrystals at the surface, but can easily be washed with water (solvent). However, AFM measurements (Fig. S9) revealed a decrease in surface roughness (from Rq= 641 nm to Rq=173 nm), suggesting minor surface modifications due to ethanol exposure or glycine deposition. This explains why a decrease in the water contact angle was observed in previous studies.

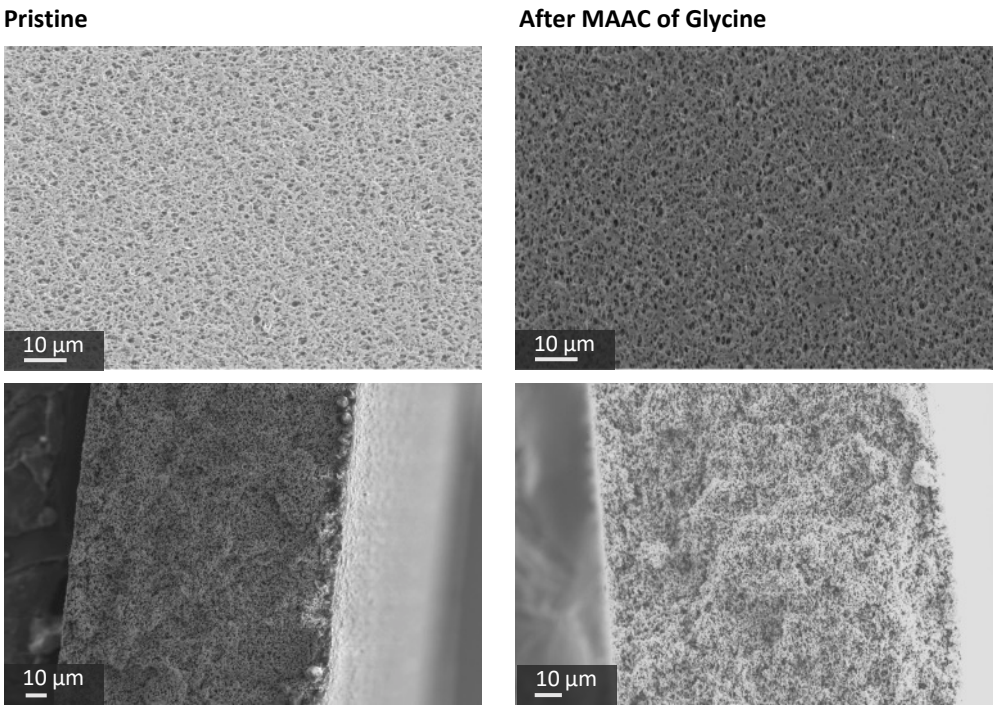

Fig. 4 SEM surface and cross-sectional images of PVDF membrane before and after the antisolvent crystallization of Glycine.

The gradual ethanol diffusion facilitated a controlled supersaturation buildup (Fig. 5a), reducing the likelihood of uncontrolled nucleation events. Supersaturation built up as ethanol concentration increased, likely promoting nucleation and crystallization. The slowing rate of supersaturation increase at later stages suggests that crystallization is occurring, consuming the excess solute. This illustrates that membrane-assisted ethanol diffusion offers a practical and reproducible strategy to modulate supersaturation buildup, thereby influencing nucleation kinetics and enabling selective polymorphic outcomes. These insights form the basis for the subsequent molecular-level investigation through MD simulations.

Based on the current study and previous research on MAAC of small molecules such as L-serine and glycine, supersaturation values have been reported to range from approximately 0.7 to 2.3 when using hydrophobic membranes like polypropylene or polyvinylidene fluoride (Fig. 5b). To better understand the molecular mechanisms by which controlled supersaturation, achieved via membrane-assisted antisolvent crystallization, affects glycine aggregation and polymorphic selection, MD simulations were conducted at supersaturation values of S = 0.74, S = 1.35, and S = 2.39.

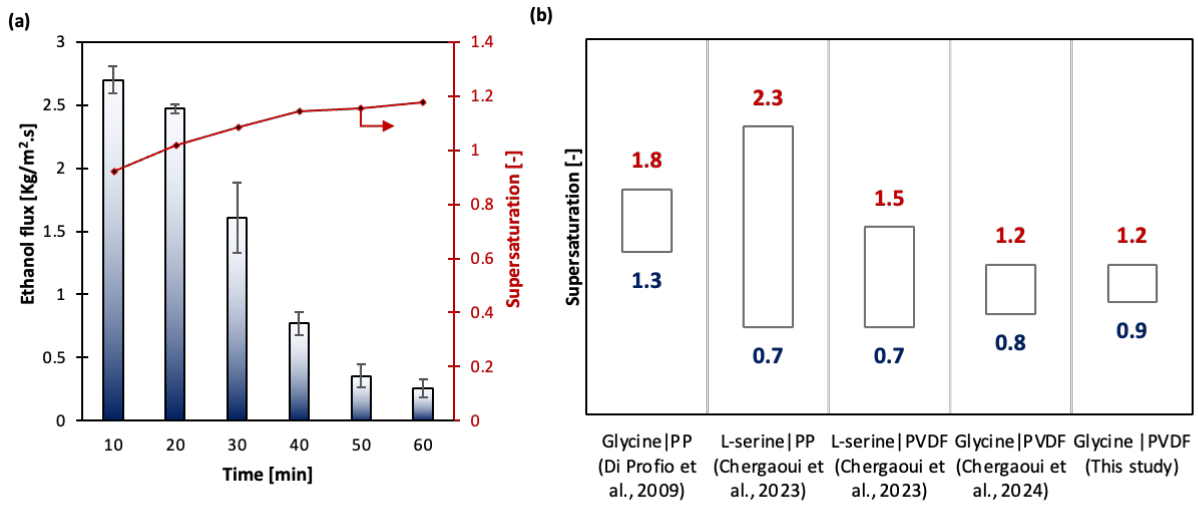

Fig. 5 (a) Evolution of the transmembrane flux of the antisolvent ethanol and corresponding supersaturation with time. Values represent mean measurements from three replicate MAAC experiments. Error estimates correspond to the standard deviation of the three replicates for each time point. (b) The range of minimum and maximum supersaturation values reported in the literature for MAAC.

3.2. Molecular Dynamics simulations

MD simulations were performed to elucidate the earliest stages of glycine aggregation under solution conditions representative of those created experimentally through membrane-assisted antisolvent crystallization. The PVDF membrane itself was not included in the molecular model. Instead, the simulations probe bulk glycine-water-ethanol mixtures at controlled supersaturation levels, enabling us to examine the molecular self-assembly pathways that are indirectly influenced in the experiments by membrane-regulated ethanol diffusion. By analyzing how supersaturation modulates dimer formation, hydrogen-bonding networks, and cluster evolution, these simulations provide mechanistic insight into the nucleation behavior underlying MAAC.

3.2.1 Crystal aggregation and growth

To quantify glycine aggregation behavior and distinguish between ordered and disordered clustering, the DBSCAN algorithm was applied to the alpha-carbons of glycine molecules in the molecular dynamics simulations (Fig. S6). DBSCAN helps identify distinct molecular crystals (clusters), enabling tracking of the early-stage organization of glycine molecules across

different supersaturation levels. This analysis provides insights into whether glycine molecules form structured pre-nucleation clusters that are potential precursors to stable crystal forms or remain disordered. The DBSCAN algorithm classifies glycine molecules into clusters based on two parameters: the maximum distance (ε = 5.58, Å) for molecular connectivity and the minimum number of molecules (η=4) required to define a cluster. These values were chosen based on the second peak of the CA–CA radial distribution function, which represents short-range glycine-glycine interactions corresponding to the typical spacing in α-glycine unit cells. In contrast, β-glycine unit cells contain only two glycine molecules, leading to a different aggregation behavior [38].

Results from DBSCAN analysis (Fig. S10) revealed that glycine aggregation occurred rapidly across all simulated supersaturation levels, with shorter induction times at higher supersaturation (Table 2). At S = 0.74, clustering occurred within 1.9 ns, whereas at S = 2.39, clustering was nearly instantaneous (<100 ps). This aligns with experimental observations of FBRM, where higher ethanol concentrations promote rapid glycine self-association, accelerating nucleation and favoring α-glycine formation.

After initial contact, glycine molecules quickly form a stable hydrogen-bond network, leading to a plateau in cluster growth. Most clustering occurs within the first two nanoseconds, after which growth stabilizes. The time to reach this plateau decreases as the number of glycine molecules increases, reflecting the supersaturation-dependent nature of nucleation kinetics.

Glycine supersaturation strongly influences the induction time (Table 2): as it increases, the induction time decreases, and the rate at which the plateau is reached increases. The induction time is inversely proportional to the number of glycine molecules in the simulation box. When the number of glycine molecules is very high, the induction time becomes undetectable, meaning that a strong hydrogen-bond network forms rapidly at the start of the simulation, connecting all the glycine molecules.

Table 2: Induction time deduced from DBSCAN simulations at incremental supersaturations.

S, -	N° Glycine	Induction time, ns
0.74	27	1.9
1.35	53	1.4
2.39	108	Not detectable (<100 ps)
1.35 no EtOH	108	Not detectable (<100 ps)

When comparing simulation results with MAAC experimental results, similar trends are observed in terms of the impact of supersaturation on glycine crystallization. The absolute timescales differ substantially because ethanol is present from the outset in the simulation box and does not require diffusion across an interface before interacting with glycine. As a result, ethanol-glycine organization proceeds much more rapidly in MD than in membrane-regulated experiments, and the aggregates formed in simulation, typically composed of only a few molecules, remain far below the size that can be detected experimentally.

Despite these differences, the molecular dynamics analysis provides direct access to the earliest stages of glycine aggregation under the specific supersaturation conditions considered in this work. Across all simulated systems, glycine molecules associate on ultrafast timescales, with detectable clusters forming within picoseconds to a few nanoseconds depending on supersaturation. Once aggregates containing at least four glycine molecules (the smallest α-like structural unit) were identified, we examined the point at which the system begins to develop internal order. To this end, we computed the orientational order parameter P_2 for two intramolecular reference vectors (Fig. S11). DBSCAN identifies clusters based on spatial proximity but not molecular orientation. The P_2 parameter complements this by quantifying alignment within clusters.

The P_2 values for the Cα–C vector, increase significantly at S = 0.74 and S = 1.35, reaching about 0.6, whereas at higher supersaturation the orientational order remains low. This behavior indicates that, under moderate supersaturation, glycine backbones partially align within the aggregates, forming locally ordered domains that can be interpreted as early precursors of crystalline nuclei. In contrast, the P_2 values associated with the Cα–N vector remain near zero across all systems, showing that the orientations of the amino groups remain largely disordered. This suggests that the hydrogen-bonding network characteristic of fully developed crystal structures has not yet emerged at this stage.

3.2.2 Molecular arrangement

To analyze glycine aggregation patterns in ethanol-water mixtures, three models containing glycine, water, and ethanol were simulated at supersaturation levels S = 0.74, S = 1.35, and S = 2.39. Additionally, one pure aqueous system (glycine and water only) at S = 1.35 was simulated for comparison. Although the total number of solute molecules stayed the same, the distribution between the crystalline and solution phases shifted during nucleation events,

498 altering the system's chemical potential. While this has little impact in the thermodynamic limit,
499 it plays a crucial role in influencing nucleation kinetics [39].

500 In the undersaturated system (S = 0.74), cyclic hydrogen-bonded glycine dimers were
501 observed (Fig. 6), forming the building blocks of α-glycine [38,40]. At S = 1.35, dimerization
502 persisted, reinforcing the idea that moderate supersaturation stabilizes ordered glycine clusters,
503 promoting α-glycine formation. However, at S = 2.39, cyclic dimers were absent, suggesting a
504 shift toward disordered aggregation, potentially favoring β-glycine formation. Literature
505 indicates that different glycine polymorphs often crystallize simultaneously from the same
506 solution, classifying them as concomitant polymorphs [41]. However, the α-polymorph is
507 commonly described as the predominant form, spontaneously crystallizing under almost any
508 experimental condition from pure aqueous solutions [42].

509 The presence of ethanol as an antisolvent significantly influenced dimer formation and
510 clustering. In ethanol-water mixtures at S = 1.35, the prevalence of cyclic dimers suggested that
511 ethanol facilitated ordered glycine assembly, stabilizing α-glycine formation. However, at S =
512 2.39, the system exhibited a lack of cyclic dimers and an increase in disordered aggregation,
513 indicating a transition to β-glycine-like structures. Even when the simulation time was extended
514 to 1000 ns (Fig. S12), no cyclic dimers were detected at S = 2.39, confirming the tendency
515 toward disordered aggregation. These observations align with experimental findings, where
516 controlled ethanol diffusion in MAAC promotes α-glycine, while rapid mixing in bulk
517 crystallization favors the formation of metastable β-glycine.

518

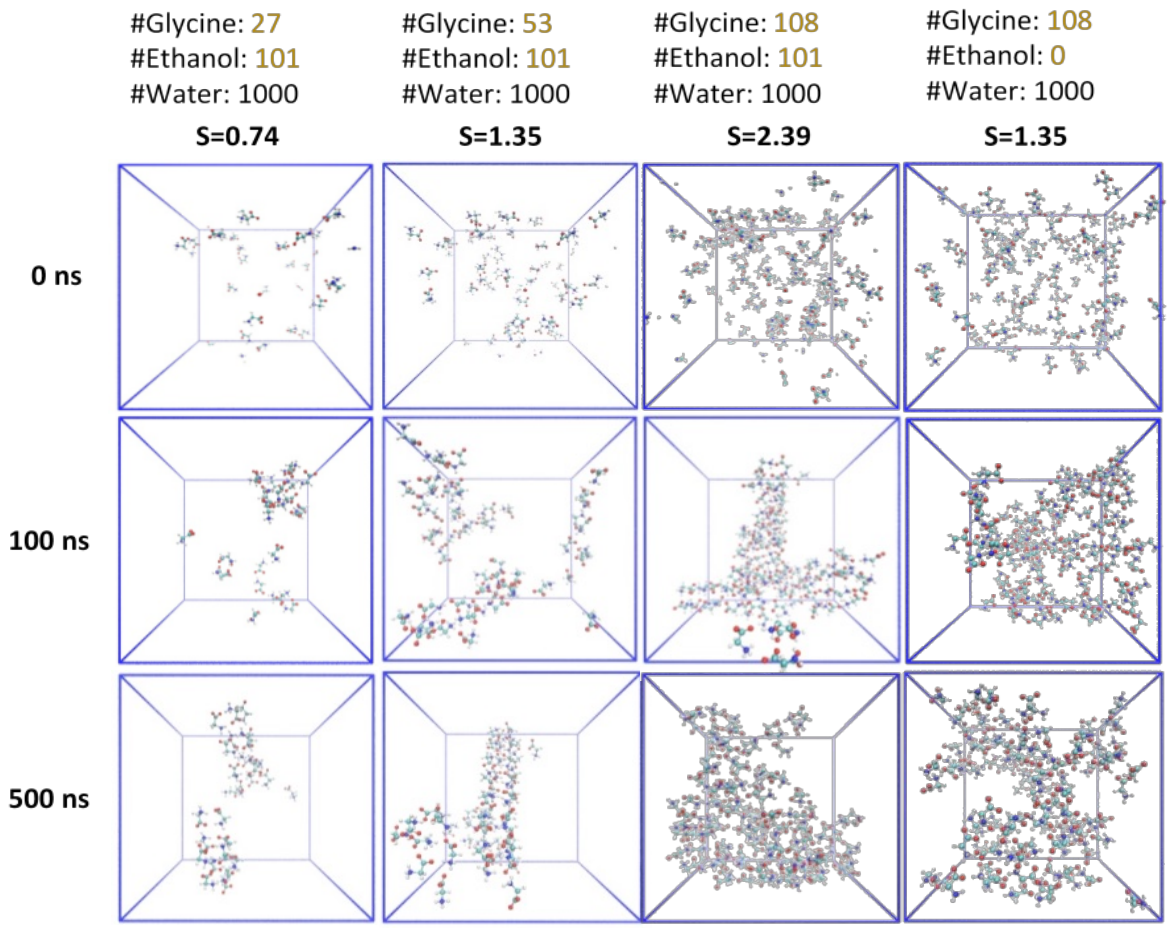

519 **Fig. 6** Arrangement of glycine molecules at 100 and 500 ns, as observed in molecular
520 dynamics simulations under different supersaturation conditions.

521

522 The influence of solvent composition on glycine aggregation is well-documented. Chen
523 *et al*., showed that methanol-water mixtures contained a higher fraction of cyclic dimers than
524 pure aqueous solutions, although this did not necessarily determine polymorphic selection
525 between α- and β-glycine [18]. Similarly, in the present ethanol-water system, variations in
526 hydrogen bonding capacity and polarity appear to modulate solute clustering, influencing
527 polymorphic selection. In the absence of ethanol, the system at S = 0.74 exhibited α-glycine
528 alongside open dimers (Fig. S13), while at S = 1.35, open-chain dimers dominated, with no
529 formation of cyclic dimers, potentially indicating β-glycine nucleation. This observation
530 supports prior studies suggesting that zwitterionic glycine molecules form either cyclic or open
531 dimers depending on solvent conditions [23]. The cyclic dimer is frequently considered the
532 structural unit of α-glycine [43], with the α-polymorph lattice consisting of bilayers of glycine
533 molecules connected by strong N-H···O hydrogen bonds [23].

Glycine polymorphism has also been linked to size-dependent stability. Parks *et al*., proposed that β-glycine nanocrystals dissolve at rates equal to or greater than those of α-glycine, regardless of particle size, indicating that β-glycine is inherently less stable in nanoscale form [44,45]. However, recent studies challenge traditional nucleation models based on the cyclic dimer hypothesis, suggesting that open-chain dimers play a crucial role in the rate-determining step of glycine nucleation [36]. This alternative molecular pathway shifts the focus from cyclic dimer stabilization to solvent-mediated nucleation mechanisms, refining our understanding of glycine polymorph selection under supersaturated conditions.

3.2.3 Glycine-Glycine Hydrogen bonding interactions

Hydrogen bonding between glycine molecules plays a fundamental role in determining polymorphic selection. The NH_3^+–COO^- hydrogen bonds are defined by an (C)O–H(N) distance of ≤ 2.2 Å and an N–H–O(C) bond angle of ≥ 140°, in line with previous computational studies [46,47]. The g(r) for glycine-glycine interactions (Fig. 7) revealed distinct hydrogen-bonding features across different supersaturation levels. The hydrogen bonds from the second to fifth peaks in the radial distribution function are depicted in Figure S12, showing distinct contributions from intra- and inter-dimer hydrogen bonds.

The first peak (r = 1.66 Å) corresponds to inter-dimer hydrogen bonds and was significantly higher in ethanol-water mixtures, indicating that ethanol promotes cyclic dimer formation. In contrast, at S = 2.39, this peak was absent, aligning with the disordered aggregation observed in the molecular arrangement analysis and correlating with the experimental formation of β-glycine under bulk crystallization conditions. The third peak (r = 2.62 Å) represents intra-molecular hydrogen bonds within individual glycine molecules, while the inter-dimer hydrogen bonding at r = 3.08 Å and the broader peaks at r = 3.70 Å and 4.38 Å suggest longer-range hydrogen bonding interactions stabilizing extended glycine networks (Table 3, Fig. S14).

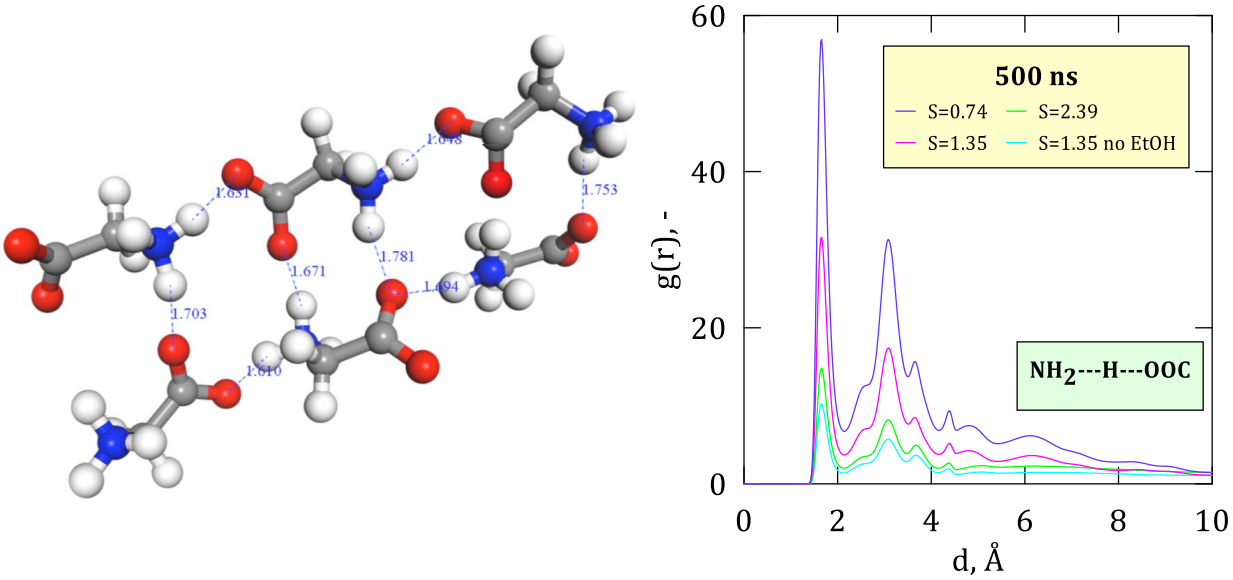

Fig. 7 Radial distribution function between the amine and carboxyl group at various supersaturations. The first peak represents the H-bonds forming intra- and inter-dimers.

Table 3: Summary of g(r) Peak Positions for Glycine-Glycine Hydrogen Bonds

S \ d(Å)	1st peak	2nd peak	3rd peak	4th peak	5th peak
0.74	1.66	2.62	3.08	3.70	4.38
1.35	1.66	2.66	3.1	3.76	4.38
2.39	1.68	2.62	3.08	3.68	4.38
1.35 no EtOH	1.64	2.60	3.08	3.66	4.36

Previous studies confirm that N–H···O=C hydrogen bonds are the primary stabilizing force in glycine clustering, with intra-dimer and inter-dimer bonds organizing cyclic dimers, which act as structural precursors to α-glycine [46]. The absence of ethanol resulted in a lower g(r) peak height, indicating that hydrogen bonding was weaker and less frequent, leading to reduced glycine aggregation in pure aqueous solutions. Ethanol's ability to increase cyclic dimer fractions suggests that ethanol-water mixtures favor α-glycine nucleation over β-glycine formation (Table S1).

3.2.4 Difference between alfa- and beta-glycine

To quantify structural differences between α- and β-glycine, the radial distribution function g(r) of Cα–Cα distances was calculated (Fig. 8a). The α-glycine structure is characterized by closed dimers, which results in a shorter Cα–Cα distance (~5 Å). In contrast,

β-glycine, composed of open dimers, exhibits greater molecular separation (>5 Å). At low supersaturation (S = 0.74), the g(r) exhibited a strong peak at 4.88 Å, indicative of α-glycine-like molecular packing. As supersaturation increased, both peak heights decreased, and at S = 2.39, the second peak at 5.58 Å became dominant, signifying an increase in β-glycine-like molecular arrangements.

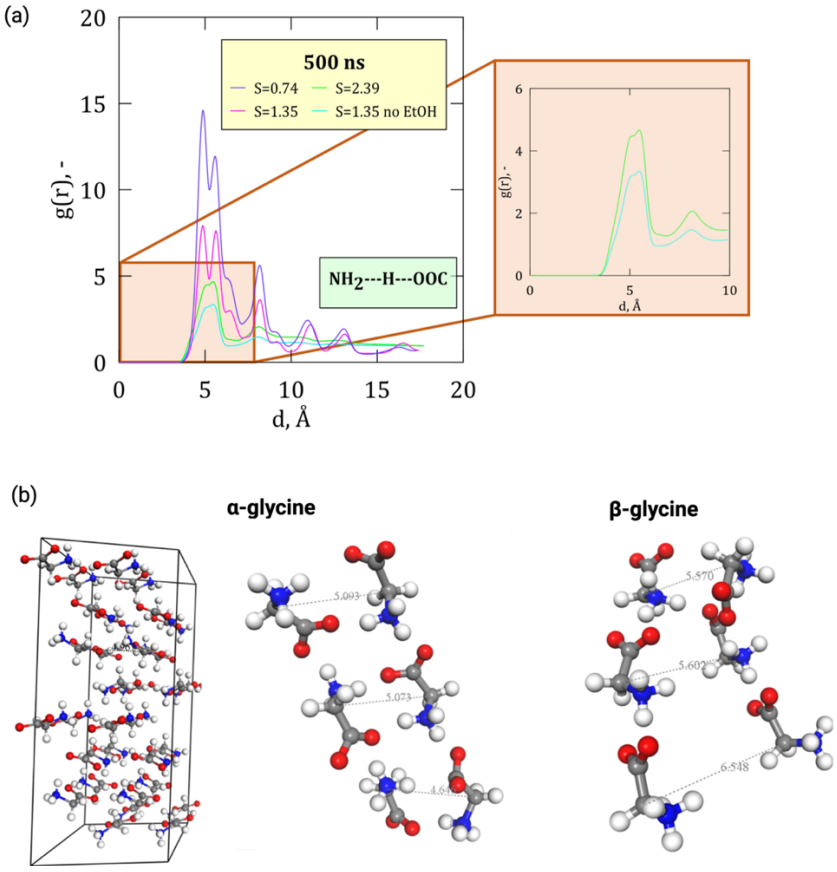

Fig. 8 Differences between α-glycine and β-glycine: (a) Radial distribution function (RDF) of α-carbon (Cα–Cα) distances at increasing supersaturation levels, highlighting structural variations, and (b) Comparative Cα–Cα distances in α- and β-glycine arrangements.

Further comparative analysis with reference α- and β-glycine structures from the Crystallography Open Database (COD) (Fig. 8b) confirmed that α-glycine maintains a consistent 5 Å spacing, while β-glycine exhibits progressive Cα–Cα elongation over time, supporting the disordered aggregation observed in MD simulations.

592 *3.2.5 Glycine-Water Hydrogen bonding interactions*

593 Water molecules serve as structural bridges during glycine crystallization. Radial
594 distribution function between the amine (-NH_3^+) and carboxyl (-COO^-) groups of glycine and
595 the oxygen in water (Fig. S15) identified three primary hydrogen bonding peaks at 1.7 Å, 3.2
596 Å, and 5.8 Å (Table 4), consistent with glycine's solvation behavior in aqueous environments.

597 Ethanol exhibited similar bonding behavior at 1.7 Å, 3.3 Å, and 6.2 Å but disrupted water
598 structuring near the glycine hydration shell, promoting desolvation and facilitating
599 crystallization [48]. The interaction pattern suggests that ethanol partially replaces water
600 molecules in glycine's first solvation shell, weakening glycine-water hydrogen bonding and
601 enhancing glycine-glycine association, promoting crystal nucleation.

602

603 **Table 4:** Summary of distances where the main peaks from g(r) of
604 carboxyl and amine group appear between glycine and water
605 molecules.

S \ d(Å)	1st peak	2nd peak	3rd peak
0.74	1.74	3.2	5.84
1.35	1.76	3.26	5.76
2.39	1.74	3.2	5.72

606

607 These simulations align with experimental findings, which show that the presence of
608 ethanol alters hydrogen bonding dynamics, shifting the balance from solvent-mediated
609 stabilization toward solute aggregation and crystallization [49,50]. Such differences can in turn,
610 influence hydrogen bonding between solute molecules, playing a crucial role in crystallization.
611 Noskov *et al.*, reported that hydrogen bonding between water molecules is disrupted near the
612 hydroxyl group, leading to an overall reduction in water hydrogen bonding within the first
613 hydration shell. This effect is primarily driven by the structuring of water in the second
614 hydration shell of ethanol [51].

615 *3.2.6 Glycine-Ethanol Hydrogen bonding interactions*

616 Ethanol plays a dual role in crystallization, acting as both a hydrogen bond donor and
617 acceptor. At low supersaturation (S = 0.74), glycine-ethanol hydrogen bonds were stronger,

stabilizing glycine in solution and delaying crystallization. As supersaturation increased (S = 1.35 and 2.39), ethanol's hydrogen bonding environment shifted, reducing glycine-ethanol interactions and promoting glycine self-association, facilitating nucleation (Fig. S16).

The radial distribution function for glycine-ethanol hydrogen bonding revealed peaks at 1.76 Å, 3.3 Å, and 6.2 Å (Table 5), indicating hydrogen bonding between ethanol's hydroxyl (-OH) and glycine's amine ($-NH_3^+$) groups. The observed trends confirm that ethanol's role as an antisolvent is concentration dependent. Low ethanol concentrations stabilize glycine in solution, whereas higher ethanol concentrations promote nucleation by reducing solvation effects.

Table 5: Summary of distances where the main peaks from rdf of carboxyl and amine group appear between glycine and ethanol molecules.

S \ d(Å)	1st peak	2nd peak	3rd peak
0.74	1.76	3.3	6.22
1.35	1.76	3.3	6.2
2.39	1.74	3.2	6.26

Previous studies have shown that at high ethanol concentrations, water tends to cluster, disrupting the hydrogen-bonded network [51]. Kitayama *et al*., further demonstrated that ethanol-induced dehydration leads to glycine clustering and crystallization, a finding that aligns well with the simulation results [17].

3.2.7 Simulation *of glycine crystallization under membrane-controlled conditions*

Membrane-assisted antisolvent crystallization (MAAC) using a PVDF membrane (Fig. S5b) [16,52,53], was investigated at S = 1.35 to examine its influence on glycine nucleation. Molecular dynamics simulations revealed that ordered glycine dimers began to form as early as 100 ns (Fig. S17), in contrast to the homogeneous bulk crystallization system, where nucleation occurred more gradually and with a greater proportion of disordered aggregates.

Although the precise role of the membrane surface remains under investigation, the results suggest that the membrane interface facilitates structured nucleation pathways. This is supported by the observation that cyclic glycine dimers, key precursors to α-glycine, were stabilized more efficiently under MAAC conditions than in conventional bulk crystallization.

Table 6 provides a direct comparison between experimental and simulation results across different supersaturation regimes, highlighting the correspondence between observed polymorphs, induction times, crystal sizes, and molecular aggregation behavior. Notably, the table also summarizes how hydrogen bonding features such as the presence of strong, ordered inter-dimer hydrogen bonds at lower supersaturation, correlate with the formation of larger, more uniform α-glycine crystals in experiments. In contrast, at higher supersaturation, the absence of cyclic dimers and the emergence of disordered hydrogen bonding networks in simulations are associated with the appearance of β-glycine and broader crystal size distributions.

The simulations reinforce experimental findings that gradual ethanol diffusion through the membrane leads to the preferential formation of α-glycine, consistent with XRD and FBRM data. The observed dimer stabilization is likely a result of the controlled mass transfer of ethanol through the membrane, which prevents supersaturation spikes and promotes gradual nucleation. This differs from bulk antisolvent crystallization, where rapid ethanol addition results in high supersaturation bursts. The absence of significant secondary nucleation in MAAC also suggests that membrane-controlled ethanol diffusion provides a more predictable crystallization pathway.

However, this small scale allows us to observe the earliest stages of crystallization in molecular-level detail, which significantly impacts the structure and properties of the resulting crystals. The simulated cluster sizes are significantly smaller than those involved in critical nucleation events, and due to the simulation time constraints, many clusters do not reach the critical nucleation threshold. Nevertheless, the early-stage molecular interactions observed in simulations provide valuable insights into solvent-mediated nucleation mechanisms, which align with experimental observations.

Table 6: Comparative summary of experimental and simulation results for glycine crystallization under membrane-assisted antisolvent conditions, including supersaturation, polymorph outcome, induction time, crystal size, molecular aggregation, and hydrogen bonding features.

Supersa-turation (S)	Polymorph (Experiment)	Polymorph (Simulation)	Induction Time (Simulation)	Crystal Size (Experiment)	Molecular Aggregation	Hydrogen Bonding Insight
0.74	α-glycine	α-glycine (cyclic dimers)	1.9 ns	-	Ordered cyclic dimers	Strong inter-dimer H-bonds (r = 1.66 Å); supports α-glycine formation
1.35	α-glycine	α-glycine (cyclic dimers)	1.4 ns	86 μm	Ordered cyclic dimers	Stable H-bond network; supports crystal growth and size uniformity
2.39	-	β-glycine-like (disordered aggregates)	<100 ps	-	Disordered aggregates	Absence of cyclic dimers; weaker H-bonding; favors β-glycine

4. Conclusions

This study demonstrates that membrane-assisted antisolvent crystallization (MAAC) offers a robust and tunable platform for controlling supersaturation and polymorph selection in glycine crystallization. By employing PVDF membranes to regulate ethanol diffusion, we achieved stable supersaturation profiles that favored the formation of α-glycine with narrow size distribution and minimal secondary nucleation. Experimental results confirmed the predominance of α-glycine through XRD and FBRM analysis, while molecular dynamics simulations revealed that cyclic glycine dimers, precursors to α-glycine, formed under moderate supersaturation, whereas disordered aggregates associated with β-glycine dominated at higher supersaturation.

The hypothesis that membrane-regulated mass transfer can modulate molecular self-assembly and polymorphic outcomes was validated through both experimental and

computational approaches. This work introduces a novel integration of MAAC with molecular simulations to elucidate early-stage nucleation mechanisms, offering mechanistic insights that are difficult to capture through conventional crystallization methods.

Compared to previous studies on bulk antisolvent crystallization [3,6,18], this work provides improved control over supersaturation kinetics and polymorph selectivity. Unlike rapid mixing systems that induce uncontrolled nucleation, MAAC enables gradual ethanol diffusion, reducing supersaturation spikes and promoting stable crystal growth [19–21]. The use of DBSCAN clustering and radial distribution function analysis further advances the molecular understanding of glycine aggregation, building on prior simulation efforts [13,18,46].

Future work will explore the extension of MAAC to more complex pharmaceutical compounds, where polymorph control is critical for bioavailability and stability. Additionally, membrane design will be optimized to tailor pore structure and surface chemistry for selective nucleation, potentially integrating stimuli-responsive materials to dynamically modulate crystallization environments.

Acknowledgments

This study is part of the PURE-20/25-108 project, titled “New Approaches in Process Intensification: Toward Integrated Purification-Reaction Membrane-Based Processes,” supported by the Actions de Recherche Concertées program and funded by the Wallonia-Brussels Federation in Belgium. The authors would like to acknowledge Frédéric Van Wonterghem from IMAP, UCLouvain, for conducting the XRD measurements. We acknowledge Tocci Lab at CNR-ITM, which provided the facilities and the mentoring necessary to conduct the MD simulations of this study. We acknowledge as well ISCRA for awarding this project access to the LEONARDO supercomputer, owned by the EuroHPC Joint Undertaking, hosted by CINECA (Italy).

References

[1]Y. Meng, Z. Qi, Z. Li, Y. Niu, M. Wu, Z. Yuan, G. He, M. Yu, X. Jiang, Tailored hydrogel composite membrane for the regulated crystallization of monosodium urate monohydrate within coffee’s metabolites system, J. Colloid Interface Sci. 648 (2023) 365–375. https://doi.org/10.1016/j.jcis.2023.05.183.

[2]L. Wang, G. He, X. Ruan, D. Zhang, W. Xiao, X. Li, X. Wu, X. Jiang, Tailored Robust Hydrogel Composite Membranes for Continuous Protein Crystallization with Ultrahigh Morphology Selectivity, ACS Appl. Mater. Interfaces 10 (2018) 26653–26661. https://doi.org/10.1021/acsami.8b08381.
[3]R. Miller, J. Sefcik, L. Lue, Modeling Diffusive Mixing in Antisolvent Crystallization, Cryst. Growth Des. 22 (2022) 2192–2207. https://doi.org/10.1021/acs.cgd.1c01269.
[4]W. Liu, S. Liu, L. Deng, X. Liang, Y. Jiang, Heterogeneous interfaces in confined microdomains of glycyrrhizic acid for polymorphism selection: Mechanisms and applications, J. Colloid Interface Sci. 682 (2025) 1017–1027. https://doi.org/10.1016/j.jcis.2024.12.012.
[5]Z. Yuan, L. Wang, M. Wu, Y. Niu, Y. Meng, X. Ruan, G. He, X. Jiang, Confined liquid crystallization governed by electric field for API crystal polymorphism screening and massive preparation, J. Colloid Interface Sci. 664 (2024) 74–83. https://doi.org/10.1016/j.jcis.2024.02.215.
[6]A. Haghighizadeh, H. Mahdavi, O. Rajabi, Recent Progress in Antisolvent Crystallization of Pharmaceuticals with a Focus on the Membrane-Based Technologies, Chem. Eng. Technol. 47 (2024) 750–763. https://doi.org/10.1002/ceat.202300412.
[7]Y. Yan, G.T. Vladisavljević, Z. Lin, H. Yang, X. Zhang, W. Yuan, PEGDA hydrogel microspheres with encapsulated salt for versatile control of protein crystallization, J. Colloid Interface Sci. 660 (2024) 574–584. https://doi.org/10.1016/j.jcis.2024.01.125.
[8]Q. Zhang, Y. Yan, Y. Xu, X. Zhang, J.W. Steed, Selective crystallization of pyrazinamide polymorphs in supramolecular gels: Synergistic selectivity by mimetic gelator and solvent, J. Colloid Interface Sci. 687 (2025) 582–588. https://doi.org/10.1016/j.jcis.2025.02.093.
[9]J. Sun, D. Bousquet, H. Forbert, D. Marx, Glycine in aqueous solution: solvation shells, interfacial water, and vibrational spectroscopy from ab initio molecular dynamics, J. Chem. Phys. 133 (2010) 114508. https://doi.org/10.1063/1.3481576.
[10] M.P. Kolesnikov, N.I. Voronova, I.A. Egorov, Molecular complexes of amino acids with porphyrins as possible precursors of pigment-protein systems, Orig. Life 11 (1981) 223–231. https://doi.org/10.1007/BF00931387.
[11] W. Zheng, J. Zhou, Z. Zhang, L. Chen, Z. Zhang, Y. Li, N. Ma, P. Du, Formation of intercalation compound of kaolinite–glycine via displacing guest water by glycine, J. Colloid Interface Sci. 432 (2014) 278–284. https://doi.org/10.1016/j.jcis.2014.06.016.
[12] I.B. Ustunol, N.I. Gonzalez-Pech, V.H. Grassian, pH-dependent adsorption of α-amino acids, lysine, glutamic acid, serine and glycine, on TiO2 nanoparticle surfaces, J. Colloid Interface Sci. 554 (2019) 362–375. https://doi.org/10.1016/j.jcis.2019.06.086.
[13] Y. Yani, P.S. Chow, R.B.H. Tan, Glycine Open Dimers in Solution: New Insights into α-Glycine Nucleation and Growth, Cryst. Growth Des. 12 (2012) 4771–4778. https://doi.org/10.1021/cg300452n.
[14] M.G. Campo, Molecular dynamics simulation of glycine zwitterion in aqueous solution, J. Chem. Phys. 125 (2006) 114511. https://doi.org/10.1063/1.2352756.
[15] Y.G. Bushuev, S.V. Davletbaeva, O.I. Koifman, Molecular dynamics simulations of aqueous glycine solutions, CrystEngComm 19 (2017) 7197–7206. https://doi.org/10.1039/C7CE01271C.
[16] M.L. Perrotta, F. Macedonio, E. Tocci, L. Giorno, E. Drioli, A. Gugliuzza, Graphene stimulates the nucleation and growth rate of NaCl crystals from hypersaline solution *via* membrane crystallization, Environ. Sci. Water Res. Technol. 6 (2020) 1723–1736. https://doi.org/10.1039/C9EW01124B.
[17] A. Kitayama, K. Kadota, Y. Tozuka, A. Shimosaka, M. Yoshida, Y. Shirakawa, Molecular aspects of glycine clustering and phase separation in an aqueous solution during anti-solvent crystallization, CrystEngComm 22 (2020) 5182–5190. https://doi.org/10.1039/D0CE00542H.
[18] J. Chen, B.L. Trout, A Computational Study of the Mechanism of the Selective Crystallization of α- and β-Glycine from Water and Methanol−Water Mixture, J. Phys. Chem. B 114 (2010) 13764–13772. https://doi.org/10.1021/jp1039496.
[19] S. Chergaoui, J. Lauzer, D.P. Debecker, T. Leyssens, P. Luis, Tuning membrane properties to control supersaturation of antisolvent crystallization, J. Membr. Sci. 694 (2024) 122415. https://doi.org/10.1016/j.memsci.2024.122415.

[20] S. Chergaoui, D.P. Debecker, T. Leyssens, P. Luis, Control of Antisolvent Mass Transfer through Porous Membranes for the Crystallization of Organic Compounds, Cryst. Growth Des. 23 (2023) 6418–6430. https://doi.org/10.1021/acs.cgd.3c00408.
[21] S. Chergaoui, D.P. Debecker, T. Leyssens, P. Luis, Key Parameters Impacting the Crystal Formation in Antisolvent Membrane-Assisted Crystallization, Membranes 13 (2023) 140. https://doi.org/10.3390/membranes13020140.
[22] B. Hess, C. Kutzner, D. van der Spoel, E. Lindahl, GROMACS 4: Algorithms for Highly Efficient, Load-Balanced, and Scalable Molecular Simulation, J. Chem. Theory Comput. 4 (2008) 435–447. https://doi.org/10.1021/ct700301q.
[23] G.A. Kaminski, R.A. Friesner, J. Tirado-Rives, W.L. Jorgensen, Evaluation and Reparametrization of the OPLS-AA Force Field for Proteins via Comparison with Accurate Quantum Chemical Calculations on Peptides, J. Phys. Chem. B 105 (2001) 6474–6487. https://doi.org/10.1021/jp003919d.
[24] D.W. Cheong, Y.D. Boon, Comparative Study of Force Fields for Molecular Dynamics Simulations of α-Glycine Crystal Growth from Solution, Cryst. Growth Des. 10 (2010) 5146–5158. https://doi.org/10.1021/cg100906s.
[25] W. Humphrey, A. Dalke, K. Schulten, VMD: Visual molecular dynamics, J. Mol. Graph. 14 (1996) 33–38. https://doi.org/10.1016/0263-7855(96)00018-5.
[26] I. Terterov, S. Koniakhin, S. Vyazmin, V. Boitsov, M. Dubina, Molecular dynamic simulations of glycine amino acid association with potassium and sodium ions in explicit solvent, F1000Research 6 (2017) 74. https://doi.org/10.12688/f1000research.10644.1.
[27] H.J.C. Berendsen, J.R. Grigera, T.P. Straatsma, The missing term in effective pair potentials, J. Phys. Chem. 91 (1987) 6269–6271. https://doi.org/10.1021/j100308a038.
[28] U. Essmann, L. Perera, M.L. Berkowitz, T. Darden, H. Lee, L.G. Pedersen, A smooth particle mesh Ewald method, J. Chem. Phys. 103 (1995) 8577–8593. https://doi.org/10.1063/1.470117.
[29] B. Hess, H. Bekker, H.J.C. Berendsen, J.G.E.M. Fraaije, LINCS: A linear constraint solver for molecular simulations, J. Comput. Chem. 18 (1997) 1463–1472. https://doi.org/10.1002/(SICI)1096-987X(199709)18:12%253C1463::AID-JCC4%253E3.0.CO;2-H.
[30] S. Nosé, A unified formulation of the constant temperature molecular dynamics methods, J. Chem. Phys. 81 (1984) 511–519. https://doi.org/10.1063/1.447334.
[31] W.G. Hoover, Canonical dynamics: Equilibrium phase-space distributions, Phys. Rev. A 31 (1985) 1695–1697. https://doi.org/10.1103/PhysRevA.31.1695.
[32] M. Parrinello, A. Rahman, Polymorphic transitions in single crystals: A new molecular dynamics method, J. Appl. Phys. 52 (1981) 7182–7190. https://doi.org/10.1063/1.328693.
[33] E. Schubert, J. Sander, M. Ester, H.P. Kriegel, X. Xu, DBSCAN Revisited, Revisited: Why and How You Should (Still) Use DBSCAN, ACM Trans Database Syst 42 (2017) 19:1-19:21. https://doi.org/10.1145/3068335.
[34] D. Chakraborty, G.N. Patey, Evidence that crystal nucleation in aqueous NaCl solution Occurs by the two-step mechanism, Chem. Phys. Lett. 587 (2013) 25–29. https://doi.org/10.1016/j.cplett.2013.09.054.
[35] D. Chakraborty, G.N. Patey, How Crystals Nucleate and Grow in Aqueous NaCl Solution, J. Phys. Chem. Lett. 4 (2013) 573–578. https://doi.org/10.1021/jz302065w.
[36] G.D. Profio, M.T. Reijonen, R. Caliandro, A. Guagliardi, E. Curcio, E. Drioli, Insights into the polymorphism of glycine: membrane crystallization in an electric field, Phys. Chem. Chem. Phys. 15 (2013) 9271–9280. https://doi.org/10.1039/C3CP50664A.
[37] K.K. Sirkar, Membranes, Phase Interfaces, and Separations: Novel Techniques and Membranes—An Overview, Ind. Eng. Chem. Res. 47 (2008) 5250–5266. https://doi.org/10.1021/ie8001952.
[38] Y. Iitaka, The crystal structure of γ-glycine, Acta Crystallogr. 14 (1961) 1–10. https://doi.org/10.1107/S0365110X61000012.
[39] Toward Stereochemical Control, Monitoring, and Understanding of Crystal Nucleation | Crystal Growth & Design, (n.d.). https://pubs.acs.org/doi/full/10.1021/cg0200560 (accessed March 21, 2024).

[40] G.L. Perlovich, L.K. Hansen, A. Bauer-Brandl, Interrelation between thermochemical and structural data of polymorphs exemplified by diflunisal, J. Pharm. Sci. 91 (2002) 1036–1045. https://doi.org/10.1002/jps.10043.
[41] J. Bernstein, R.J. Davey, J.O. Henck, Concomitant Polymorphs, Angew. Chem. Int. Ed Engl. 38 (1999) 3440–3461. https://doi.org/10.1002/(sici)1521-3773(19991203)38:23%253C3440::aid-anie3440%253E3.0.co;2-%2523.
[42] S. Polat, P. Sayan, Effect of ultrasonic irradiation on morphology and polymorphic transformation of glycine, Ultrason. Sonochem. 47 (2018) 17–28. https://doi.org/10.1016/j.ultsonch.2018.04.013.
[43] C.S. Towler, R.J. Davey, R.W. Lancaster, C.J. Price, Impact of Molecular Speciation on Crystal Nucleation in Polymorphic Systems: The Conundrum of γ Glycine and Molecular 'Self Poisoning', J. Am. Chem. Soc. 126 (2004) 13347–13353. https://doi.org/10.1021/ja047507k.
[44] B.D. Hamilton, M.A. Hillmyer, M.D. Ward, Glycine Polymorphism in Nanoscale Crystallization Chambers, Cryst. Growth Des. 8 (2008) 3368–3375. https://doi.org/10.1021/cg800326a.
[45] C. Parks, A. Koswara, H.-H. Tung, N.K. Nere, S. Bordawekar, Z.K. Nagy, D. Ramkrishna, Nanocrystal Dissolution Kinetics and Solubility Increase Prediction from Molecular Dynamics: The Case of α-, β-, and γ-Glycine, Mol. Pharm. 14 (2017) 1023–1032. https://doi.org/10.1021/acs.molpharmaceut.6b00882.
[46] S. Hamad, C.E. Hughes, C.R.A. Catlow, K.D.M. Harris, Clustering of Glycine Molecules in Aqueous Solution Studied by Molecular Dynamics Simulation, J. Phys. Chem. B 112 (2008) 7280–7288. https://doi.org/10.1021/jp711271z.
[47] C.E. Hughes, S. Hamad, K.D.M. Harris, C.R.A. Catlow, P.C. Griffiths, A multi-technique approach for probing the evolution of structural properties during crystallization of organic materials from solution, Faraday Discuss. 136 (2007) 71–89. https://doi.org/10.1039/B616611C.
[48] A.V. Dighe, P.K.R. Podupu, P. Coliaie, M.R. Singh, Three-Step Mechanism of Antisolvent Crystallization, Cryst Growth Des (2022).
[49] C.D. Zeinalipour-Yazdi, E.Z. Loizidou, An experimental FTIR-ATR and computational study of H-bonding in ethanol/water mixtures, Chem. Phys. 550 (2021) 111295. https://doi.org/10.1016/j.chemphys.2021.111295.
[50] T.A. Dolenko, S.A. Burikov, S.A. Dolenko, A.O. Efitorov, I.V. Plastinin, V.I. Yuzhakov, S.V. Patsaeva, Raman Spectroscopy of Water–Ethanol Solutions: The Estimation of Hydrogen Bonding Energy and the Appearance of Clathrate-like Structures in Solutions, J. Phys. Chem. A 119 (2015) 10806–10815. https://doi.org/10.1021/acs.jpca.5b06678.
[51] S.Yu. Noskov, G. Lamoureux, B. Roux, Molecular Dynamics Study of Hydration in Ethanol−Water Mixtures Using a Polarizable Force Field, J. Phys. Chem. B 109 (2005) 6705–6713. https://doi.org/10.1021/jp045438q.
[52] Influence of Polyvinylidene Fluoride Polymorphs in Membrane-Assisted Crystallization: NaCl Crystals Nucleation and Growth, (n.d.). http://www.genchemistry.org/EN/10.21127/yaoyigc20200015 (accessed April 2, 2024).
[53] M.L. Perrotta, F. Macedonio, L. Giorno, W. Jin, E. Drioli, A. Gugliuzza, E. Tocci, Molecular insights on NaCl crystal formation approaching PVDF membranes functionalized with graphene, Phys. Chem. Chem. Phys. 22 (2020) 7817–7827. https://doi.org/10.1039/D0CP00928H.

All figure captions

Figure_1 Schematic of the set-up used to evaluate membrane-regulated crystallization. An in-line FBRM probe was installed at 45˚ in the crystallizing solution to continuously track the chord length. [Intended for color production]

Figure_2 Representation of the boundary layer conditions depending on the antisolvent transmembrane flux: either nucleation is solely related to the direct contact of the antisolvent and crystallizing solution (a) or is additionally impacted by the heterogeneous nucleation from the membrane surface (b). [Intended for color production]

Figure_3 Crystal shape and morphology obtained with MAAC (a), crystalline structure (b), FBRM chord count with time (c), and chord length distribution (d). [Intended for color production]

Figure_4 SEM surface and cross-sectional images of PVDF membrane before and after the antisolvent crystallization of Glycine. [Intended for color production]

Figure_5 (a) Evolution of the transmembrane flux of the antisolvent ethanol and corresponding supersaturation with time (b) The range of minimum and maximum supersaturation values reported in the literature for MAAC. [Intended for color production]

Figure_6 Arrangement of glycine molecules at 100 and 500 ns, as observed in molecular dynamics simulations under different supersaturation conditions. [Intended for color production]

Figure_7 Radial distribution function between the amine and carboxyl group at various supersaturations. The first peak represents the H-bonds forming intra- and inter-dimers. [Intended for color production]

Figure_8 Differences between α-glycine and β-glycine: (a) Radial distribution function (RDF) of α-carbon (Cα–Cα) distances at increasing supersaturation levels, highlighting structural variations, and (b) Comparative Cα–Cα distances in α- and β-glycine arrangements. [Intended for color production]